

# Spectral Evidence for Widespread Galaxy Outflows at $z > 4$

Brenda Frye<sup>1</sup>

*Department of Astrophysical Sciences, Princeton University, Peyton Hall, Princeton, NJ  
08544*

Tom Broadhurst

*Racah Institute of Physics, The Hebrew University, Jerusalem, Israel 91904*

and

Narciso Benítez

*Department of Physics and Astronomy, Johns Hopkins University, 3400 N. Charles Street,  
Baltimore, MD 21218-2686*

## ABSTRACT

We present discovery spectra of a sample of eight lensed galaxies at high redshift,  $3.7 < z < 5.2$ , selected by their red colors in the fields of four massive clusters: A1689, A2219, A2390, and AC114. Metal absorption lines are detected and observed to be blueshifted by 300-800 km s<sup>-1</sup> with respect to the centroid of Ly- $\alpha$  emission. A correlation is found between this blueshift and the equivalent width of the metal lines, which we interpret as a broadening of saturated absorption lines caused by a dispersion in the outflow velocity of interstellar gas. Local starburst galaxies show similar behavior, associated with obvious gas outflows. We also find a trend of increasing equivalent width of Ly- $\alpha$  emission with redshift, which may be a genuine evolutionary effect towards younger stellar populations at high redshift with less developed stellar continua. No obvious emission is detected below the Lyman limit in any of our spectra, nor in deep  $U$  or  $B$ -band images. The UV continua are reproduced well by early B-stars, although some dust absorption would allow a fit to hotter stars. If B-stars dominate, then their relatively prominent stellar absorption lines should separate in wavelength from those of the outflowing gas, requiring more detailed spectroscopy. After correcting for the lensing, we derive small physical sizes for our objects,  $\sim 0.5$ -5 kpc

---

<sup>1</sup>NSF Astronomy and Astrophysics Postdoctoral Fellow

$h^{-1}$  for a flat cosmology with  $\Omega_m = 0.3, \Omega_\Lambda = 0.7$ . The lensed images are only marginally resolved in good seeing despite their close proximity to the critical curve, where large arcs are visible and hence high magnifications of up to  $\sim 20\times$  are inferred. Two objects show a clear spatial extension of the Ly- $\alpha$  emission relative to the continuum starlight, indicating a “breakout” of the gas. The sizes of our galaxies together with their large gas motion suggests that outflows of gas are common at high redshift and associated with galaxy formation.

*Subject headings:* cosmology: gravitational lensing — cosmology: observations — galaxies: clusters: individual (Abell 2390, 2219, 1689, AC114) — galaxies: distances and redshifts

## 1. Introduction

The photometric selection of high redshift galaxies by their Lyman-limit break has proven to be a successful means of obtaining galaxy redshifts in the range  $2.5 < z < 3.3$  (Steidel & Hamilton 1992; Steidel et al. 1996a,b; Lowenthal et al. 1997). At somewhat higher redshift, photometric selection is less reliable because the forest depression of the continuum between Ly- $\alpha$  and the Lyman limit can be confused with evolved or dusty galaxies at lower redshift. Moreover, these Lyman-depressed galaxies at  $z\sim 4$  are significantly fainter than the Ly-break galaxies, making spectroscopic work challenging. Despite this, a sample of 48 *B*-band dropout selected galaxies has been spectroscopically confirmed by Steidel et al. (1999). These are observed with relatively low spectral resolution, sufficient for determining redshifts in the range  $3.8 < z < 4.5$ , and occur with a frequency consistent with little evolution relative to the lower redshift Ly-break galaxies (Steidel et al. 1999).

Only a handful of higher redshift galaxies are known, the best examples being serendipitous discoveries boosted by lensing (Warren et al. 1996; Franx et al. 1997; Trager et al. 1997; Frye & Broadhurst 1998). Others are identified primarily on the basis of an asymmetric emission line taken to be Ly- $\alpha$  (Dey et al. 1998), or by virtue only of a relatively large lower limit for the equivalent width of single emission lines (Weymann et al. 1998; Hu et al. 1998; Hu et al. 1999; Stern et al. 2000a; Rhoads et al. 2000; Manning et al. 2000). In principle, high quality photometry alone is sufficient for  $z>4.5$  candidates because the strength of the Lyman-series forest depression (Madau 1995) can be established from bright QSO spectra (Schneider et al. 1989; Storrie-Lombardi et al. 1996), yielding precise predictions about the galaxy colors at those redshifts. This continuum suppression feature has led to convincing claims of  $z>5$  for the very reddest objects in the Hubble Deep Field (Lanzetta et al. 1996; Spinrad et al. 1998), and more recently, to the successful selection of high redshift QSOs

by Stern et al. (2000b) and the Sloan Digital Sky Survey collaboration (Fan et al. 2000; Anderson et al. 2001, and references therein).

Here we make use of this established high redshift Lyman-series depression to color select galaxies for spectroscopy near the critical curves of some of the most massive lensing clusters. This approach provides a viable way of obtaining useful spectroscopy of high- $z$  galaxies, under favorable circumstances, where lensing is compounded by a massive cluster galaxy lying close to the critical curve of a cluster (Franx et al. 1997; Frye & Broadhurst 1998).

The galaxies presented here form part of a systematic redshift survey of red-selected galaxies behind massive lensing clusters. Most galaxies selected in this way are early type lying at modest redshift behind the cluster. We present the full redshift survey, and measurements of cluster masses by magnification, in a different paper (Frye et al. 2001). Here we show only the most distant galaxies discovered in our survey as a by-product of the red selection, and whose optical colors place them in the range  $3.5 < z < 6.5$  (Benítez 2000). We analyze the spectral information from 8 lensed galaxies detected with redshifts of  $z = 3.77, 4.04, 4.07, 4.25, 4.46, 4.67, 4.87,$  and  $5.12$ . These objects are relatively bright, allowing for detailed spectroscopic work, and are suitable for follow-up at other wavelengths.

This paper is organized as follows. In §2 we describe the target selection and in §3 we outline the photometric and spectroscopic observations and data analysis techniques. This is followed by a presentation of the photometric and spectroscopic results in §4, an examination of the agreement with photometric redshift results in §5, and an analysis of gas motion and the equivalent width of the Ly- $\alpha$  emission line in §6. We close in §7 with a discussion of our main results.

## 2. Target Selection

The lensing clusters were chosen to have the largest possible critical radii and to lie at relatively low redshift so as to maximize the number of background galaxies redder than the cluster early type sequence. Most of our color-selected galaxies have modest redshifts,  $0.4 < z < 1.2$  (Frye et al. 2001), but a small number turn out to be forest-depressed high redshift galaxies. Four clusters were used: A1689 ( $z=0.18$ ), A2390 ( $z=0.23$ ), A2219 ( $z=0.23$ ), and AC114 ( $z=0.31$ ). These are massive, X-ray luminous lensing clusters which show giant arcs and examples of multiply lensed images (Figs. 3, 7, 8).

Target selection for spectroscopy is based on color and not on elongated morphologies. This is because in general relatively circular mass substructure can create apparently undis-

torted images (*e.g.* Trager et al. (1997)). Also, in the case of intrinsically small sources, the elongation by lensing may still leave an object poorly resolved even with Hubble Space Telescope (HST) resolution (for this reason lensed QSOs do not appear arc shaped). This is demonstrated, for example, in Fig 5, which shows the galaxy at  $z=4.868$  along with its ground based *UBVIJ* images. The object lies close to a giant arc and is therefore highly magnified, by  $\sim 10\times$ , but is only marginally resolved spatially due to its intrinsically small size.

The minimum color for our selection is set by the upper envelope of early type cluster members, which is sharply defined and varies between clusters as a result of the k-correction (Kaiser et al. 1995). At  $z>4$ , Ly- $\alpha$  falls longward of the *V* band so that a color difference between *V* and *I* will be apparent. At  $z=4.5$  the continuum depression amounts to  $\sim 2$  magnitudes in *V* (Fig. 1).

### 3. Observations

#### 3.1. Imaging and Photometry

The magnitudes quoted here are SExtractor MAGBEST magnitudes (Bertin & Arnouts 1996), or for the very compact objects, aperture magnitudes corrected to ‘total’ magnitudes using stellar aperture corrections. We used the following imaging data for making our photometric measurements and target selections.

##### 3.1.1. A2219

We have obtained deep observations on Keck I with the Low Resolution Imaging Spectrometer (LRIS) in July, 1996 in good seeing  $\sim 0''.7$  (Oke et al. 1995), totalling 20 min in *V* and 10 min in *I* (Fig. 8). Two giant arcs frame the very large cluster member just below and west of center, with many other arclets seen about the bright central galaxies.

##### 3.1.2. A1689

We obtained deep *V* and *I* band observations at the European Space Observatory (ESO) New Technology Telescope (NTT) in 1995. In 1999 we obtained new deep *V*, *R*, *I*, and *Z* data taken in average seeing of  $0''.8$  with LRIS at Keck II. The largest arc is shown in Fig 3, subtending 30 degrees around the cluster center. Many other giant arcs are visible at

this radius, following a contour encompassing the bright central galaxies. The photometric redshift analysis presented in §5 is based on these data plus additional  $U$  band observations with the Du Pont telescope at Las Campanas,  $B$  band observations with the Nordic Optical Telescope at La Palma, and deep  $J, H, K$  imaging taken at ESO NTT with the Son of ISAAC (SOFI) IR imaging spectrograph. The reduction and analysis of these  $UBVRIZJHK$  data will be presented in an upcoming paper (Benítez & Broadhurst 2002).

### 3.1.3. *A2390*

The imaging data were taken at the Canada France Hawaii Telescope in  $V$  and  $I$ , and for the core region, archival HST images were analyzed in  $V$  and  $I$  (Squires et al. 1996; Frye & Broadhurst 1998). The righthand panel in Fig. 7 and the color plate in Frye & Broadhurst (1998) show the arcs at  $z=4.04$  and other giant arcs in the center of this cluster.

### 3.1.4. *AC114*

The imaging data were taken at the Anglo Australian Telescope, consisting of approximately 3 hours of imaging in the  $B$  and  $I$  bands. For this cluster, the color selection was based only on these two bands.

## 3.2. Spectroscopy

### 3.2.1. *A1689*

Some of the spectroscopic observations were carried out with LRIS on the Keck I telescope in June 1997, totalling 2h 43min through a  $1''.0$  slit and in seeing of  $0''.6-0''.8$ . The 300 line/mm grating was used blazed at  $5000\text{\AA}$ , resulting in a resolution of  $12\text{\AA}$  at  $6000\text{\AA}$ , determined from unblended sky lines. Adequate relative spectrophotometry is obtained by taking the spectrum of an early type cluster member at  $z=0.187$ , observed simultaneously through the multislit mask, and comparing it to the standard empirical E/SO spectrum of Kennicutt (1992). These observations resulted in the detection of three high redshift galaxies at  $z=3.77$ ,  $z=4.87$ , and  $z=5.12$ , shown in Figs. 4, 5, and ?? respectively.

More spectroscopic observations of these and other red selected galaxies behind A1689 were made with LRIS on Keck II in March and April 1999, totalling 2h 20min and 2h 05min respectively, through a  $1''.0$  slit, and in good seeing of  $\sim 0''.8$  on both occasions. The

400 line/mm grating was used blazed at  $6700\text{\AA}$ , resulting in a resolution of  $10\text{\AA}$  at  $6000\text{\AA}$ , determined from unblended sky lines. Relative spectrophotometry for the  $z=4.868$  galaxy is obtained using the same fluxing curve established for the June 1997 data. Although fairly rough, the fluxing curve is found to be smooth across the throughput, leaving the spectral features unaffected and therefore adequate for the purposes of our redshift survey. This set of observations resulted in additional observations for the objects at  $z=3.770$  and  $z=5.120$ .

In total, three high- $z$  galaxies were discovered behind A1689, with exposure times of 3h 40min ( $z=5.12$ ), 4h 40min ( $z=4.87$ ) and 2h 20min and 3h 40min ( $z=3.77$ ).

### 3.2.2. A2219

The spectroscopy for the three high- $z$  galaxies behind A2219 was taken with LRIS on Keck II in August 1998 in 5h 40min of exposure with the 400 line grating (Figs. 9, 10, 11). The slit width was  $1''$ , resulting in a resolution of  $10\text{\AA}$  and a dispersion of  $1.8\text{\AA}/\text{pix}$ . We observed the spectrophotometric standard G24-9 under photometric conditions, providing a relative flux calibration.

### 3.2.3. A2390

The spectroscopy for the one dimensional spectrum for the  $z=4.039$  galaxy behind A2390 (Fig. 7) was taken with LRIS on Keck I in June 1997 in 2hr 50min of exposure, and is described in a previous paper (Frye & Broadhurst 1998). Further longslit spectroscopy at higher spectral resolution was also obtained with Keck I in June 1997, whose two dimensional spectrum is shown in the lower panel of Fig 7.

### 3.2.4. AC114

The spectroscopy for the high- $z$  galaxy at  $z=4.248$  behind AC114 was taken with LRIS on Keck II in August 1997 in 2hr 8min of exposure with the 300 line grating blazed at  $5000\text{\AA}$ . The slit width was  $1''$ , resulting in a resolution of  $12\text{\AA}$  at the blazing angle, determined from unblended sky lines.

### 3.3. Reductions

We developed our own IDL reduction software to handle the large number of spectra efficiently ( $\sim 40$  targets per multislit mask with 3-6 exposures per mask), and to address issues relating to pronounced flexure and other spectral image artifacts (see §3.3.2 and §3.3.3 below). Our aim is to maximize the signal-to-noise without resampling the data, so that groups of pixels carrying faint continuum signal have every chance of being detected as a coherent pattern in the final reduced image. Although purpose built, the code is general and can be applied to single and multislit data. It is also fast and convenient, processing the raw fits files directly.

#### 3.3.1. Reduction Procedure

The reduction procedure begins by flattening the data via dome or superflats, as available. White light dispersed flatfields or ‘object flats’ are used to take out the wavelength dependent effects of the pixel response. Cosmic ray events are removed by  $\sigma$ -clipping above a suitable threshold which depends mainly on the number of independent exposures. Fringing changes between the exposures, and therefore is not removed completely by the dome flat, requiring dithering the spectra along the slit to average away this problem at long wavelengths ( $> 7500\text{\AA}$ ).

Spatial curvature corrections are important for tracking the object plus background accurately, amounting to up to 5 pixels from center to end of a slitmask (see §3.3.2). Its proper characterization allows for the detection of the faintest objects, where the continuum signal is not readily identified before one dimensional extraction but can be located blindly with knowledge of the spatial curvature plus the known device coordinates of the mask and targets. We identify cosmic rays incident on the data frames by flagging the hottest members in each spatial column with the median, and then by fitting low order polynomials and applying iterative  $\sigma$ -clipping. The mean value of the good background pixels is then subtracted from the image.

The spectra typically have a relatively limited coverage of sky, with on average only 10-40 pixels in a given spatial column with which to determine the best estimate. In these cases, and on account of the spectral tilt, sky subtraction is achieved by correcting for a gradient in the spatial direction of the sky values (see §3.3.2 below). This distortion results in a slowly changing gradient in sky values in the spatial direction which we fit with a low order polynomial. We find that since many more independent sky pixels are averaged over in this way than in the standard procedure for sky subtraction this leads to a more accurate

correction, eliminates the need for rebinning, and produces higher signal-to-noise results.

The wavelength calibration is obtained accurately from the many bright sky lines in the red, and the choice of lines is interactively improved on with a cursor connection. The 1d spectra are then extracted without resampling, and following the spatial curvature. Cosmic rays on the object are flagged in one dimension, by  $\sigma$ -clipping relative to the local continuum, and then removed across a stack of exposures by interactive  $\sigma$ -clipping. Thresholds are set for acceptable number of cosmic ‘hits’ per pixel stack, to avoid removal of real spectral features.

### 3.3.2. *Curvature Correction*

#### *Following the Curvature*

The data are distorted in the spatial direction with respect to the 2d detector frame. We find that we can remove this 2d curvature without repixelization by following the curvature of the initially straight slit boundaries which lie between the multislit spectra on the slitmask. At each boundary the pixel values abruptly drop from the sky value of typically  $\sim 200$  counts per pixel down to zero, providing a well defined curvature. We fit it with a low order polynomial and then shift the solution onto the object spectrum. We then sum up the object signal in the dispersion direction, shifting the entire pixel stack along spatially by on average 3-5 pixels from center to end of the mask, as determined by the polynomial. In this way we avoid rectifying the 2d image or introducing noise into the background-limited data. Note for its ability to follow background-limited objects over the full dispersion range, we advise this approach over the conventional one of following the curvature of the object itself.

#### *Spectral Tilt*

While good flatfielding may average out the background sky, it does not account for a slow wavelength variation in the spatial direction. This type of curvature imposes a tilt on the spectrum which is most pronounced on the edges of the bright sky lines. Here the large change in signal from the background value to emission peak introduces an increment-decrement pattern, resulting in an artificial P-Cygni type profile that depends slowly on wavelength. In between the sky lines this effect can be traced well with a slowly varying polynomial. Operationally, we fit a linear slope in the spatial direction to each spatial pixel stack which is determined by smoothing over a running boxcar along the dispersion direction to get a good local estimate. This procedure of treating the sky as a smoothly varying 2D surface is found to improve the signal-to-noise of the data considerably for sections lying



between the sky lines.

For bright sky lines, however, the slope in the spatial direction is determined for each column and then subtracted, since the gradient of the sky values is very steep and depends sensitively on where the sky line lies with respect to the fixed pixel grid. Although only one column is used at a time, this estimate is a fair one because the sky lines are relatively bright. Note that this process does not require rebinning of the data, unlike the conventional approach of rectifying the entire 2D frame with arc-lamp calibrations.

### 3.3.3. Artifacts

Both punched and milled masks produce physical defects along the slits, imprinting dark and bright spatially-dependent striations into the data. The resulting artifacts of this nonuniform illumination typically affect the background by 3-5%, enough to lose background-limited spectra completely for an unlucky alignment where an object falls into a trough. The effect is much worse for the punched masks, which were used in about one third of the experimental runs. The effect can be corrected for, to first order, by dividing the object flats into the data, but, as with the fringing correction, small time dependent changes occur that limit the usefulness of the flatfield.

The spatial profile of the slit, or slit function, is complex, varying on subpixel scales. The sampling of the slit function in the spatial direction varies along the spectrum due to the curvature, and therefore offers in principle the opportunity to define this function over different pixel phases. In this way one potentially can piece together a well sampled function and apply it to the data. Although this algorithm is not part of the standard reduction code, it has been used in some of the more gross examples of non-uniform illumination.

## 4. Results

A total of eight high redshift galaxies were discovered as a consequence of our  $V - I$  color selection and these are listed in Table 1, 2. details. Table 1 gives the imaging details in five columns: cluster name; position in J2000 coordinates;  $I_{AB}$  magnitude and its  $1\sigma$  error;  $(V - I)_{AB}$  color; and lensing corrected size, in  $\text{kpc h}^{-1}$  for a flat cosmology with  $\Omega_m = 0.3, \Omega_\Lambda = 0.7$ . Table 2 gives the spectral details in six columns: cluster name, redshift (not heliocentric corrected); rest equivalent width of Ly- $\alpha$ ; summed rest equivalent width of OI $\lambda$ 1302 + SiII $\lambda$ 1304; summed rest equivalent width of SiII $\lambda$ 1260 + OI $\lambda$ 1302 + SiII $\lambda$ 1304 + CII $\lambda$ 1336; and velocity shift between the centroid position of Ly- $\alpha$  and the absorption

lines.

The apparent magnitudes of these objects are relatively bright owing to the large magnifications,  $23 < I_{AB} < 25$ , producing relatively high quality spectra (Figs. 4, 5, 6, 7, 9, 10, 11, and 12). The redshifts are clearly all high, for which the Lyman series redshifts into the  $V$  band, suppressing the flux in  $V$  relative to  $I$  and giving these high- $z$  galaxies their characteristically large colors of  $V_{AB} - I_{AB} \geq 1.5$  (Fig. 1). In addition, the  $J$ -band image detects our brightest high redshift example easily (Fig. 5).

The results are organized as follows. In §4.1 we describe the continuum models generated for comparison with the data, in §4.2 we give the error estimation, in §4.3 we give the prescription for estimating the magnification, and in §4.4 we present the spectra and images.

#### 4.1. Continuum Modelling

Stellar continuum fits are compared with the fluxed spectra. The model is composed of a single stellar spectral type, which we find is sufficient for estimating the continuum shapes and determining the relative line velocities. Continuum light in the UV sampled at high redshift is of course dominated by the hottest stars for any reasonable initial mass function (IMF), given the steep dependence of luminosity on temperature for opaque material (de Mello et al. 2000). A more detailed fit to our data, using spectral synthesis models, will be presented elsewhere. Kurucz models with solar metallicities were used to estimate the temperature of the dominant contribution to the UV at restframe  $\sim 1000\text{\AA}$ , where we sample their spectra (Kurucz 1993). Reddening is expected to be important at short wavelengths, as is underscored by the presence of metal lines in all of the high redshift galaxies in our sample. The effects of reddening and/or age variations on the colors and continuum shapes may be constrained with the help of infrared information.

We include sources of opacity into the models as necessary. The requisite Lyman-series opacity, as defined by Haardt & Madau (1996), is found to match the data well (Fig. 5). Our highest signal-to-noise data also require an HI opacity at the source, with column densities of HI between  $\log N = 21.1$  and  $\log N = 21.5$  (Figs. 9, 10, 11).

The hot B-stars which typically give good fits to the continuum also show an intrinsic Ly- $\alpha$  absorption which can dilute an otherwise strong Ly- $\alpha$  emission. This becomes increasingly more pronounced for late B-stars, where the absorption increases strongly with decreasing temperature. Fig. 11 shows one of our model fits to the data. Here we fit a simple two component model consisting of a B3 star plus Lyman-series opacity. Continuum fitting in this detail has not been possible for comparably high redshift galaxies (Dey et al. 1998; Hu

et al. 1998), for which the continuum is only marginally detected at best, or in the case of the  $z=4.92$  lensed galaxy of Franx et al. (1997), its continuum is contaminated by light from a nearby cluster member.

## 4.2. Error Estimation

Error estimates on the equivalent width of Ly- $\alpha$  emission and its wavelength centroid are made with respect to the above continuum models, in an attempt to deal with a potentially large gradient in the continuum light profile under this line, due to HI absorption local to the galaxy and potentially from stellar atmospheres. Hence, there is most likely a sizable systematic uncertainty in the equivalent width of this line and also some smaller error on the central velocity. The uncertainty in the model then is the main source of error, which we have included in Table 2.

As the equivalent width is measured with respect to the bestfit model, the errors we quote on it are based on the uncertainty in the normalization of the bestfit model. A  $1\sigma$  estimate of the continuum height is determined simply by the absolute value of the dispersion of the continuum in each wavelength bin about the mean continuum level, excluding sky pixels and the ends of the spectrum. This dispersion measure is then corrected downward by a factor representing the square-root of the number of useful wavelength bins over which the continuum fit is made. The equivalent width is then remeasured, shifting the normalization up and down by this error in normalization. For the absorption lines, the continuum height is better determined locally, as the continuum gradient is rather flat in general for these lines and so the standard manual technique of continuum and line selected spectral regions is adopted and the error again is assumed to be dominated by the uncertainty on the continuum fit.

The centroid velocity is less sensitive to the choice of model and is determined simply from an intensity weighted first moment of the wavelength integrated over a restricted range of wavelength which is somewhat subjectively determined by the quality of the data but covering typically not much more than about twice the spectral resolution of  $\sim 10\text{\AA}$ . In most cases the emission line is not evidently well resolved and hence the central wavelength largely reflects the instrumental resolution and over sampling of our data by a factor of about 6 for each wavelength bin relative to the resolution for the 400-line grating.

For the absorption lines, the centroid velocity is determined using a local fit to the continuum height and, in the usual way, the flux-weighted wavelength centroid is determined relative to the local continuum level. The error on the velocity centroid is close to the

sampling limit of  $1.8\text{\AA}$  or  $\approx 70 \text{ km s}^{-1}$  for the best defined lines. A purely empirically determined estimate can also be obtained by comparing the redshifts from the different absorption lines. In this case the dispersion is somewhat larger than the sampling,  $\approx 110 \text{ km s}^{-1}$ , on average, providing an average internal estimate. The larger of these two numbers we quote for  $\Delta V$  in Table 2, where the dispersion is determined for each spectrum individually in the case where more than one absorption line redshift can be measured.

### 4.3. Magnification Estimation

The main uncertainty in estimating the magnification of an image is the gradient of the lensing mass profile. The flatter the profile, for a fixed Einstein ring radius  $\theta_E$ , the greater the magnification. For a power law mass density profile  $\Sigma \propto \theta^{-p}$ , where  $p$  is the power law index, we may expect the slope to lie in the range  $0.5 < p < 1$ , bracketing the projected singular isothermal profile and the Navarro, Frenk, and White (NFW) slope near the Einstein ring thought to be appropriate for a large cold dark matter halo (Navarro et al. 1995).

It is relatively straightforward to obtain a useful expression for the magnification at angular position  $\theta$ ,  $\mu(\theta)$ , in terms of  $\theta_E/\theta$ :

$$\mu(\theta)^{-1} = \left[1 - \left(\frac{\theta_E}{\theta}\right)^p\right] \left[1 - (1-p)\left(\frac{\theta_E}{\theta}\right)^p\right]$$

For highly magnified images close to the Einstein radius ( $\theta_e \approx \theta$ ), this reduces to

$$\mu(\theta) \approx \frac{1}{p^2} \frac{1}{(1 - \theta_E/\theta)}$$

In terms of the magnification by a singular isothermal lens, it becomes  $\mu(\theta) \approx \frac{1}{p^2} \mu^{iso}$ . Thus, without a precise determination of the central slope  $p$  it is not possible to obtain an accurate estimate of the magnification.

This magnification correction can be applied to the fluxes and to the sizes of the spatially resolved objects. Note in the cases where only the lensed major axis is resolved, as is typical of the objects in our sample, then one measures the magnification via the tangential stretch factor,  $\mu_t$ . This is just the first part of the above product for  $\mu(\theta)^{-1}$ , and is hence a smaller correction yielding a lower limit on the magnification:

$$\mu_t(\theta)^{-1} = \left[ 1 - \left( \frac{\theta_E}{\theta} \right)^p \right]$$

Close to the Einstein ring this becomes,

$$\mu_t \approx \frac{1}{p} \left( \frac{1}{1 - \theta_E/\theta} \right)$$

In terms of the tangential stretch factor for the isothermal case,  $\mu_t \approx \frac{1}{p} \mu_t^{iso}$ . Hence, this correction is inversely dependent on the slope of the mass profile for images close to the Einstein ring.

In the following section we provide fluxes corrected for lensing by the factor  $\mu(\theta)$ , and intrinsic sizes corrected for lensing by the factor  $\mu_t(\theta)$ , covering what we assume to be the range of plausible central slopes of  $0.5 < p < 1.0$ . Note that the Einstein radius  $\theta_E$  is safely assumed to lie very close to the angles subtended by the main giant arcs seen in each cluster, on account of the low redshifts of the clusters selected,  $z \approx 0.2$ . This is because the distance ratio,  $d_{ls}/d_s$ , of source-lens separation is very similar to the source distance and hence the bend angle of light has a negligible dependence on redshift for our purposes.

#### 4.4. Individual High-z Detections

Each high-z detection will be discussed in turn below. In the main panel of each figure we show the signal versus observed wavelength on the lower axis and restframe wavelength on the upper axis. Continuum models are compared with the data, where relevant (see §4.1). The sky spectrum is included at the bottom of the panel in order to evaluate the reliability of the spectrum more clearly. It varies markedly with wavelength due to the presence of many bright sky lines and fringing in the red. We attach a postage stamp image of each object in two or more of the *UBVIJ* bands, and center the object in the overlaid circle. Magnifications are computed and used to estimate the unlensed flux and intrinsic size (see §4.3). Note that the objects are typically only marginally resolved, resulting in upper limits on the sizes and lower limits on the magnitudes. We measure sizes for a flat cosmology with  $\Omega_m = 0.3, \Omega_\Lambda = 0.7$ .

#### 4.4.1. A1689

$$z=3.770$$

The image and spectrum for this multiply lensed object are shown in Figs. 3, and 4 respectively. A shallower, blue spectrum appears in the lefthand panel and a deeper, higher resolution one on the right. The spectrum shows very weak or absent Ly- $\alpha$  emission, for which we quote an upper limit on the equivalent width of  $\sim 3$  Å. Both the Ly- $\alpha$  and Ly- $\beta$  breaks are detected, and several metal lines are clearly identified as SiII $\lambda$ 1260, OI and SiII at  $\lambda$ 1302 and  $\lambda$ 1304 respectively, CII $\lambda$ 1336, and SiIV $\lambda$ 1398 and  $\lambda$ 1402, from which we determined the redshift.

This object is obviously elongated by lensing (see image in righthand panels), forming a tangential arc of angular size  $2.2''$ . The object lies about  $15''$  outside the Einstein ring, resulting in a tangential magnification of 6-12 and a flux magnification of 6-24 for the uncertain slope in the range  $0.5 < p < 1$ . This yields an intrinsic size of  $\approx 1.5$ - $2.5$  kpc  $h^{-1}$  and an unlensed magnitude in the range  $26 < I_{AB} < 27.5$  (see Table 1).

$$z=4.868$$

The image of our brightest object,  $I_{AB} = 23.3$ , is shown in Fig. 3, and its fluxed spectrum in Fig. 5. From the emission line, readily identified as Ly- $\alpha$ , a distinctive break on the blueward side and the clear presence of an absorption line at  $7396$  Å, identified as SiII $\lambda$ 1260, we determined the redshift. Ly- $\alpha$  is redshifted by  $360 \pm 70$  km  $s^{-1}$  from the metal line, and is obviously asymmetric with a more extended wing on the red side. Such a profile shape is now established as a common property of all high- $z$  galaxies where Ly- $\alpha$  is seen and the data are of sufficient quality (Franx et al. 1997; Frye & Broadhurst 1998; Dey et al. 1998; Pettini & et al 2001).

A distinctive wedge-like step shortward of Ly- $\beta$  is observed, as predicted at high redshift (Madau 1995), and caused by the increasing opacity of the Lyman-series forest for wavelengths greater than that of Ly- $\beta$  at the emission redshift. A good continuum fit is found to a late type B0 star (see §4.1). This is considerably bluer than the B3 and B5 best fits to our other high- $z$  spectra (Figs. 9, 10, 11, and Fig. 2 in Frye & Broadhurst (1998)).

No significant flux is seen in the spectrum below the Lyman limit and no emission is detected in the  $U$  and  $B$  bands down to our  $2\sigma$  limiting magnitudes of  $U_{AB} = 27.3$  and  $B_{AB} = 26.7$  (see also Fig. 5), indicating that no significant flux has escaped below the Lyman limit, at least along our line of sight. A more detailed determination of the escape fraction will be published elsewhere. A deficit of continuum flux below the Lyman limit is

not unexpected for any galaxy in which star formation is centrally concentrated. Of course in addition, any modest column lower redshift intervening forest cloud in the range  $z > 4.3$  could also lead to a non-detection in the  $U$  and  $B$  bands.

This is the reddest object measured in the field,  $(V - I)_{AB} > 3.2$ , and almost redder than a passively evolving elliptical is expected to reach at maximum, near  $z=1$  (See Fig. 1). Our deep ground based image resolves the object in  $I$  in seeing of  $0''.8$ , and detects it at the  $3\sigma$  level in  $J$ .

The intrinsic size of the object can be determined roughly by its position relative to the Einstein radius, which we take to be  $\theta_E = 50''$  given by the main arc (Fig. 3). The lensed image lies  $\sim 20''$  outside this radius, resulting in a tangential stretch factor of 3-7 and a flux magnification of 3-14 for a slope in the range  $0.5 < p < 1$ . This yields an intrinsic size of  $\approx 1-2 \text{ kpc h}^{-1}$  and an unlensed magnitude in the range  $24.7 < I_{AB} < 26.2$ .

$$z=5.120$$

The highest redshift object in our sample lies at  $z=5.120$  (Fig. 3) and its spectrum is shown in Fig. 6. From the strong asymmetric emission line detected at  $7430 \text{ \AA}$  (see inset), and a distinctive break on the blueward side we determined the redshift. The line has an obviously asymmetric profile and the largest observed equivalent width of our sample,  $W_\alpha \sim 30 \text{ \AA}$ . Identified as Ly- $\alpha$ , we tentatively find absorption at the expected position of SiIII $\lambda$ 1260 at the  $\sim 2.5\sigma$  level. Our deep imaging provides a lower limit of  $(V - I)_{AB} > 1.5$ , with  $I_{AB} = 25.2$  and a  $2\sigma$  upper limit of  $V_{AB} > 26.5$ . Below the galaxy and sky spectrum are the images in  $U, B, V, I$ , and  $J$ . The object appears clearly only in the  $I$  band, where it is faint and unresolved. No flux is seen in the spectrum below the Lyman limit.

The magnification of this object is hard to determine with any precision because it lies so close to the critical curve, within  $5''$ , where the magnification diverges. It is interesting that despite the very large magnification, which must be in excess of  $\mu > 10$ , the object is at best only marginally spatially resolved, meaning that its luminous part is intrinsically very small, of order  $0''.7/\mu$  or  $< 0.5 \text{ kpc h}^{-1}$  for the flat case. We estimate an unlensed apparent magnitude of  $I_{AB} > 27.5$ .

#### 4.5. A2390

$$z=4.039$$

The image and fluxed spectrum for this multiply lensed object is shown in Fig. 7 and is discussed in detail in a previous paper (Frye & Broadhurst 1998). The prominent features detected are the Lyman-series and Ly- $\beta$  breaks, and an asymmetric Ly- $\alpha$  emission line which is redshifted by  $420 \text{ km s}^{-1}$  with respect to the clearly detected interstellar absorption lines of SiII  $1260\lambda$ , OI and SiII at  $1302$  and  $1304$  respectively, and CII $1336$ . Also SiIV $1398$  and  $1402$  are detected and shown in Fig. 2 of Frye & Broadhurst (1998).

The righthand panel shows the HST WFPC 2 color image constructed in the F606W and F814W passbands, from which we clearly distinguish four spatially stretched image components and individual HII regions along the  $5''$  and  $3''$  long N and S components respectively (see Fig. 7). In addition, there is cluster elliptical in the center of the inset image which has been removed with a deVaucouleur’s profile to reveal the four image components of this ‘extended’ Einstein cross.

We have constructed a simple isothermal lens model which provides an adequate fit to the data. It consists of a dominant central cluster potential modified by the cluster member galaxy that splits the images (Frye & Broadhurst 1998). The magnification is hard to constrain well since the images lie so close to the critical curve where the magnification diverges. The HST images allow a reasonable estimate of the size of this object given by the width of the lensed images in the radial direction which is little affected by lensing if the slope is close to isothermal. The measured width is  $0.2''$  (Frye & Broadhurst 1998), corresponding to an intrinsic size of  $\sim 1 \text{ kpc h}^{-1}$  for the flat case.

#### 4.6. A2219

$$z=4.068$$

This object is labelled in Fig. 8 and its fluxed spectrum shown in Fig. 9. The spectrum has several strong and nearly saturated metal lines which are identified as SiII $1260$ , OI $1302$  SiII $1304$ , CII $1336$ , and SiIV $1398$  and  $1402$ , from which we determined the redshift. There is a broad absorption which we take to be absorption by the A-band at  $7600 \text{ \AA}$ . Ly- $\alpha$  is seen in emission and is redshifted by  $830 \text{ km s}^{-1}$  with respect to the metal absorption lines, indicating a substantial amount of gas outflow. The best fitted model is for a B5 stellar population (solid line) with Lyman-series forest attenuation along the line of sight and an HI column at the source of  $\log N = 21.1$ . The Lyman-series break appears shortward of Ly- $\alpha$



and no flux is detected below the Lyman limit in the spectrum. The  $V$  and  $I$  band images in the righthand panels show the object to be faint,  $I_{AB} = 24.1$ , and a  $V$ -band dropout. The magnification is likely to be small since the object is at  $\sim 15$  critical radii, resulting in only a  $\sim 10\%$  correction to the observed magnitude and size.

$$z=4.445$$

The object at  $z=4.068$  is labelled in Fig. 8 and its fluxed spectrum is shown in Fig. 10. It is a high quality spectrum with a signal-to-noise of  $\sim 7$  per pixel in the continuum. The most prominent features are the strong interstellar metal lines and the sharp Ly- $\alpha$  break. Ly- $\alpha$  is seen in emission and has a characteristically asymmetric shape extending to the red. This is likely to be a dynamical effect as we discuss in §6.1. The centroid of Ly- $\alpha$  is shifted redward by  $\sim 700$  km s $^{-1}$  with respect to the clearly identified lines of SiII $\lambda$ 1260, OI $\lambda$ 1302, SiII $\lambda$ 1304, CII $\lambda$ 1336, and SiIV $\lambda$ 1398 and  $\lambda$ 1402, from which we determined the redshift. The best fitted model is for a B3 stellar population (solid line) with Lyman-series forest attenuation along the line of sight and an HI column at the source of  $\log N = 21.1$ . The object is detected in both the  $V$  and  $I$  images shown to the right of the spectrum.

The magnification of the image is modest, as it lies about 3 critical radii from the center, resulting in a tangential stretch factor of  $< 3$  and a flux magnification of  $< 6$  for the uncertain slope in the range  $0.5 < p < 1$ . The intrinsic size is estimated to be  $\sim 2 - 4$  kpc h $^{-1}$  for the flat case, and its unlensed magnitude to be in the range  $24 < I_{AB} < 25.5$ .

$$z=4.654$$

The object at  $z=4.654$  is labelled in Fig. 8 and its fluxed spectrum is shown in Fig. 11. The signal to noise is good, reaching  $\approx 4$  in the continuum at relatively high spectral dispersion of 1.8 Å/pixel. Ly- $\alpha$  is in emission and has a clearly asymmetric shape. Shortward of this, a sharp break is seen taken to be the Lyman-series break. The interstellar metal line SiII $\lambda$ 1260 is clearly detected in this spectrum, and other lines commonly found in high- $z$  galaxies are marked. From the emission line, continuum break, and absorption line we determined the redshift. Note that the broad absorption line at  $\lambda 7600$  Å we take to be absorption by the A-band.

Somewhat surprisingly, the stellar continuum rises redward of the Ly- $\alpha$  emission line instead of declining as would be expected from a hot stellar population with no absorption at the source. This feature is also seen in the slightly higher signal-to-noise spectrum at  $z=4.445$  in Fig. 10, and may be caused entirely by HI absorption at the emission redshift or by the combined effect of HI opacity and the stellar population.

The best fitted model is a B3 stellar population (solid line) which has been attenuated by the Lyman-series forest and damped HI absorption with column density  $\log N = 21.5$  placed at the emission redshift. There is a broad absorption which we take to be absorption by the A-band at  $\lambda 7600 \text{ \AA}$ . The centroid of the Ly- $\alpha$  emission line is shifted towards the red by  $425 \text{ km s}^{-1}$  with respect to this line, and has a total rest equivalent-width of  $W_{Ly\alpha} \sim 16 \text{ \AA}$ . The  $V$  and  $I$  band images at the position of this arc are shown on the righthand side of the spectrum with a flux of  $I_{AB} = 24.9$  and a color of  $(V - I)_{AB} > 2.1$ . The angular size in  $I$  is small and unresolved.

The magnification is not large as this object lies at about 4 critical radii, resulting in a tangential stretch factor of 1.5-3 and a flux magnification of 1.5-5 for the uncertain slope in the range  $0.5 < p < 1$ . The intrinsic size is estimated to be  $< 2 \text{ kpc h}^{-1}$  for the flat case, and the unlensed apparent magnitude,  $I_{AB} > 25.2$ .

#### 4.7. AC114

*4.248*

The image and spectrum of the object at  $z=4.248$  is shown in Fig. 12. The spectrum shows a strong Lyman-series absorption shortward of the position of Ly- $\alpha$ , weak Ly- $\alpha$  emission, and a marginal detection of the interstellar line SiII $\lambda$ 1260 ( $2\sigma$  level), from which we determined the redshift. The Ly- $\alpha$  emission line is redshifted by  $460 \text{ km s}^{-1}$  with respect to the metal line. The restframe equivalent width for Ly- $\alpha$  has an upper limit of  $W_{\alpha} = 3 \text{ \AA}$ . The  $B$  and  $I$  band images in the righthand panels show that the object centered in the circles is faint,  $I_{AB} = 23.9$ , and a  $B$ -band dropout. Note that the bluer band for this object is  $B_{AB}$  and not the usual  $V_{AB}$ , as we did not obtain  $V$ -band data for this cluster.

This image lies about  $20''$  outside of the Einstein radius, resulting in a tangential stretch factor of  $2.5 - 5$  and a flux magnification of  $2.5 - 10$  for the uncertain slope in the range  $0.5 < p < 1$ . The intrinsic size is estimated to be  $< 2 \text{ kpc h}^{-1}$  for the flat case, and its unlensed magnitude to be in the range  $24.9 < I_{AB} < 26.4$ .

### 5. Consistency with Photometric Redshifts

As described in §3, we have obtained optical imaging in the  $UBVRIZJH$  and  $K$  bands for A1689, and very high quality photometric redshifts have been determined for this field using the Bayesian method of Benítez (2000). We compare the galaxy colors with those

of a forest opacity corrected redshifted template set, formed by the main spectral types of Coleman et al. (1980), plus two starbursts from Kinney et al. (1996). We take into account the intrinsic color variation or ‘cosmic variance’ in the galaxy colors by convolving the resulting color likelihoods with a gaussian of width  $0.06(1+z)$ , empirically measured from the Hubble Deep Field (HDF) (Benítez 2000). This makes the range of final redshift probabilities considerably wider than they would be if we included only the photometric error, but it yields a more accurate representation of the true uncertainties involved in the estimation. Since we are working on a cluster field which strongly magnifies the observed flux from background objects, we use the redshift magnitude prior  $p(z|T, m)$  introduced in Benítez (2000) for field galaxy distributions, but with the corresponding *unlensed* magnitude, as calculated in §4.

The photometric redshifts estimated for the high- $z$  objects in the A1689 field are shown in Fig 2 and give excellent agreement with the spectroscopic ones. This is also true for the full spectroscopic survey sample, and with this new photometry we have identified even higher redshift targets out to  $z \sim 6.5$ , for which spectroscopic follow-up is being carried out with the Very Large Telescope (VLT).

## 6. Analysis

### 6.1. Gas Motion

#### 6.1.1. Velocity Dispersion

In the spectrum of each object the metal line equivalent widths and the velocity shift of the Ly- $\alpha$  centroid with respect to these metal lines is measured (Table 2, Fig. 13). There is an additional observation made for our object at  $z=4.04$  (Bunker et al. 2000). The analysis yielded an independent velocity shift measurement which confirmed our original measurement of  $420 \text{ km s}^{-1}$  (Frye & Broadhurst 1998), and so is not included separately here.

Similar measurements from other high quality spectra are compiled from the literature for comparison (Leitherer et al. 1996; Franx et al. 1997; Lowenthal et al. 1997; Kunth et al. 1998). The results are shown graphically for a local plus high- $z$  sample (Fig. 14), and high- $z$  sample only (Fig. 15). The former includes only the two metal lines in common to all the samples, OI 1302 $\lambda$  and SiII 1304 $\lambda$ . A fairly clear trend emerges in that the blueshift of the metal lines relative to the centroid of the Lyman- $\alpha$  emission correlates with the equivalent width of metal line absorption. Doppler broadening by the gas motion would leave the equivalent width unaltered for the optically thin case. However, if the lines are optically

thick, as we may expect for interstellar gas, then the width will be proportional to the velocity dispersion. The appearance of saturation is obvious in the spectra for the two objects in our survey at  $z=4.068$  and  $z=4.445$  in A2219 (Fig. 9 and 10). In other cases it is not directly clear although our limited spectral resolution is responsible for smoothing away the core of lines of equivalent width less than the resolution of  $\sim 12\text{\AA}$ . Also we may expect that the spatial coverage of dense gas does not fully cover the starlight continuum, so that the light which is not absorbed partially fills the line.

Hence, for saturated absorption lines, a spread in gas velocity broadens the line and we propose that the trend we find in Figs. 14 and 15 is just a consequence of an intrinsic spread in the dispersion in the gas outflow velocity. This in turn increases the equivalent width of the absorption lines and the mean outflow velocity, thereby generating a larger blueshift of the metal lines with respect to the systemic velocity. Note that the velocity width of the absorption lines is only marginally resolved in the best cases with our limited spectral resolution.

In addition to our data, blueshifts of the metal lines have also been measured for the gravitational ring discovered by Warren et al. (1996), in which the wavelengths of the IR emission lines have been compared with Ly- $\alpha$ . The same use of IR lines has been achieved for 15 relatively bright  $z\sim 3$  U-dropout galaxies by Pettini & et al (2001). They argue that restframe optical lines may better represent the systemic velocity of the galaxy, rather than the resonantly scattered Ly- $\alpha$  line. Perhaps the cleanest measure of the mean expansion rate is a comparison of IR lines with metal absorption lines, for which most of their objects in that paper have measurements (their Fig. 13). The velocities lie in the range  $+200$  to  $-500$  km s $^{-1}$ , and are in fact very similar in magnitude to the velocity offset between Ly- $\alpha$  and the metal lines.

### 6.1.2. Models

Legrand et al. (1997) convincingly explain the discrepancy in velocity of the metal lines relative to Ly- $\alpha$  as arising from back scattered Ly- $\alpha$  photons either emitted from the expanding HII region or scattered from the inner ‘wall’ of the surrounding HI, so that the Doppler redshift of far side emission is sufficiently large to clear it in wavelength of foreground absorption within the galaxy along the line of sight. For the galaxies in which Ly- $\alpha$  emission is absent, comprising about half the local starburst galaxies and distant  $z > 2.5$  galaxies (Steidel et al. 1996a,b; Steidel et al. 1999), correspondingly strong Ly- $\alpha$  absorption is seen. From this we deduce that the most likely cause is a combination of a lower rate of internal expansion and/or a higher HI column for absorption, rather than simply absorption by dust.

In locally well studied examples of starburst galaxies with obvious outflowing gas, Heckman et al. (1998) measure larger outflows for the face on cases. Since the galaxies at high redshift tend to be either elongated by lensing or smaller than the seeing disk, it is difficult to obtain inclination information.

## 6.2. Equivalent Width of Ly- $\alpha$ Emission

We find a tentative trend in the equivalent width of Ly- $\alpha$  versus redshift across our range  $3.7 < z < 5.2$  (Fig. 16). This is potentially a genuine evolutionary effect towards younger stellar populations at high redshift at which time the stellar continuum level will be lower because fewer stars have been created. The time evolution of the equivalent width of Ly- $\alpha$  during a star formation episode has been investigated in detail for single burst models with a Salpeter IMF and a constant star formation rate (Bruzual & Charlot 1993; Valls-Gabaud 1993). Here a large equivalent width of  $W_{Ly\alpha} = 250 \text{ \AA}$  is expected during the first  $10^{6.5}$  years, when the stellar continuum builds up to a constant level given by the lifetime of the hottest stars. After this point, the equivalent width declines, and after  $10^7$  years is expected to be found in absorption due to the filling in by Ly $\alpha$  absorption from B stars. Dust will of course reduce the ionizing flux further.

The main uncertainty on the estimate of the equivalent widths in faint sky dominated spectra arises from uncertainty in the continuum level underneath the emission line (see §4). Our continuum models are used to calculate this and show that depending on the stellar population and the degree of absorption close to Ly- $\alpha$  this can be quite large.

With all this in mind, if the formation rate of galaxies is significantly increasing during our observed redshift interval, then we might be witnessing genuine evolutionary behavior. On the other hand, selection effects may be at work at some level. We may have missed galaxies which lie at the higher redshift end of our sample but for which the equivalent width of Ly- $\alpha$  is low due the effects of a small internal expansion rate or dust. Clearly this is a potentially interesting result requiring larger samples of distant galaxies for a fuller description.

## 7. Discussion and Conclusions

The claimed absence of Ly- $\alpha$  emission in deep narrowband searches (Thompson & Djorgovski 1995) was readily explained by dust absorption along the hugely increased path length of resonantly scattered Ly- $\alpha$  emission (Charlot & Fall 1993), for even relatively modest

columns of neutral hydrogen. However, the recent discovery of copious numbers of high redshift galaxies at  $2.5 < z < 3.5$ , half of which show Ly- $\alpha$  in emission (Steidel et al. 1999; Rhoads et al. 2000), revises this conclusion.

The explanation for the escape of Ly- $\alpha$  emission is plausibly explained as a dynamical effect from outflowing gas, based on detailed UV spectroscopy of nearby starburst galaxies (Legrand et al. 1997). This outflow model, although not yet quantified, can account for the peculiar observations reported here and for other high quality spectra of high redshift galaxies. The Ly- $\alpha$  photons generated by hot stars in the center of HII regions can escape if back scattered from the inner “wall” of the surrounding expanding gas, thereby avoiding the fate of the average Ly- $\alpha$  photon which scatters and then is absorbed by dust within the surrounding gas. These redder, back scattered photons take on the outflow velocity. If great enough, this velocity will exceed in wavelength the redward wing of Ly- $\alpha$  absorption of the foreground gas through which these photons must pass in order to reach the observer. In contrast, the bluer photons will be preferentially absorbed, leading to an asymmetric emission line.

The internal gas motion implied by the mismatch of interstellar absorption lines with emission lines of Ly- $\alpha$  and non-resonance lines of OI detected in the IR has established, by analogy with local starburst galaxies, that gas outflows are ubiquitous at early times. If this gas escapes the potential of these early galaxies, then the consequences for galaxy formation are predicted to be rather important.

The gas belonging to neighboring density perturbations which have not yet virialized will be only tenuously held and be expected to be stripped away by winds from nearby collapsed starforming galaxies (Scannapieco & Broadhurst 2001a). Since galaxy formation is predicted to be much more spatially correlated at early times by biasing (Cole & Kaiser 1989), the effect locally is to suppress the formation of small galaxies (Scannapieco & Broadhurst 2001b). At later times, this metal enriched gas is expected to become bound to larger density perturbations which take longer to collapse and will be heated and further enriched, modifying the cooling times of massive galaxies and clusters (Scannapieco & Broadhurst 2001b).

The ubiquitous presence of metals in the IGM detected out to the highest redshifts that the forest has been probed (Frye et al. 1993; Lu et al. 1996a,b), and the high level of enrichment of cluster gas, may be most easily explained by a general pollution by early galaxies (Scannapieco & Broadhurst 2001a; Madau et al. 2001; Pettini & et al 2001) though other mechanisms have been proposed to contribute, including tidal stripping of processed gas (Gnedin & Ostriker 1997), and photoevaporation of gas in sufficiently small galaxies by UV background (Barkana & Loeb 2000b).

Lensing helps to spatially resolve galaxies by stretching their images so that one can obtain intrinsic size measurements. We have made this calculation for several of our highly magnified cases, which after the correction for the likely level of magnification show that the objects are in fact very small,  $\sim 0.5\text{-}5 \text{ kpc h}^{-1}$ . This is in reasonable agreement with a sample of very distant red objects identified in the HDF fields (Spinrad et al. 1998; Weymann et al. 1998). It also agrees with theoretical predictions (Barkana & Loeb 2000a) for the early evolution expected in the hierarchical models for structure formation, in which the first galaxies to form are small, with increasingly more massive objects collapsing and merging over time.

We conclude that the lensed galaxies presented here provide high quality information on the earliest known galaxies. Lensing has fortuitously afforded us detailed spectral and spatial details of magnified but presumably otherwise typical examples of galaxies at  $z > 4$ . The rarity of luminous high redshift galaxies and the requirement of a high magnification for useful spectroscopic follow-up means that such work will be slow but well rewarded with precious data on galaxies at otherwise inaccessibly early times.

We are grateful to Hy Spinrad for advice and to Richard Ellis, Garth Illingworth, Tim Heckman, and Alex Kim for helpful conversations. We thank Warrick Couch for valuable assistance in reducing the AC114 data. We thank Bev Oke and Judy Cohen for providing the LRIS instrument, and recognize the expert assistance of several of the staff at the Keck Observatories, including David Sprayberry, Randy Campbell, Bob Goodrich, Barbara Schaefer, Terri Stickel, Gary Puniwai, Ron Quick, and Wayne Wack, and Greg Wirth. The W. M. Keck Observatory is a scientific partnership between the University of California and the California Institute of Technology, made possible by the generous gift of the W. M. Keck Foundation. Finally, we thank the anonymous referee for a careful reading of the manuscript.

## REFERENCES

- Anderson, J. et al. 2001, AJ, submitted, astro-ph/0103228
- Barkana, R. & Loeb, A. 2000a, ApJ, 531, 613
- . 2000b, ApJ, 539, 20
- Benítez, N. 2000, ApJ, 536, 571
- Benítez, N. & Broadhurst, T. 2002, ApJ, in Prep.

- Bertin, E. & Arnouts, S. 1996, *A&AS*, 117, 393
- Bruzual, A. G. & Charlot, S. 1993, *ApJ*, 405, 538
- Bunker, A. J., Moustakas, L. A., & Davis, M. 2000, *ApJ*, 531, 95
- Charlot, S. & Fall, S. M. 1993, *ApJ*, 415, 580+
- Cole, S. & Kaiser, N. 1989, *MNRAS*, 237, 1127
- Coleman, G. D., Wu, C. ., & Weedman, D. W. 1980, *ApJS*, 43, 393
- de Mello, D. . F., Leitherer, C., & Heckman, T. M. 2000, *ApJ*, 530, 251
- Dey, A., Spinrad, H., Stern, D., Graham, J. R., & Chaffee, F. 1998, *ApJ*, 498, L93
- Fan, X. et al. 2000, *AJ*, 120, 1167
- Franx, M., Illingworth, G. D., Kelson, D. D., van Dokkum, P. G., & Tran, K.-V. 1997, *ApJ*, 486, L75
- Frye, B. L., Bechtold, J., Moustakas, L. A., & Dobrzycki, A. 1993, *MNRAS*, 263, 575+
- Frye, B. L. & Broadhurst, T. J. 1998, *ApJ*, 499, 115
- Frye, B. L., Broadhurst, T. J., Guhathakurta, P., & Benítez, N. 2001, *ApJ*, in preparation
- Gnedin, N. Y. & Ostriker, J. P. 1997, *ApJ*, 486, 581+
- Haardt, F. & Madau, P. 1996, *ApJ*, 461, 20+
- Heckman, T. M., Robert, C., Leitherer, C., Garnett, D. R., & Van Der Rydt, F. 1998, *ApJ*, 503, 646+
- Hu, E. M., Cowie, L. L., & McMahon, R. G. 1998, *ApJ*, 502, 99
- Hu, E. M., McMahon, R. G., & Cowie, L. L. 1999, *ApJ*, 522, L9
- Kaiser, N., Squires, G., & Broadhurst, T. 1995, *ApJ*, 449, 460+
- Kennicutt, R. 1992, *ApJ*, 388, 310
- Kinney, A. L., Calzetti, D., Bohlin, R. C., McQuade, K., Storch-Bergmann, T., & Schmitt, H. R. 1996, *ApJ*, 467, 38



- Kunth, D., Mas-Hesse, J. M., Terlevich, E., Terlevich, R., Lequeux, J., & Fall, S. M. 1998, *A&A*, 334, 11
- Kurucz, R. 1993, ATLAS9 Stellar Atmosphere Programs and 2 km/s grid. Kurucz CD-ROM No. 13. Cambridge, Mass.: Smithsonian Astrophysical Observatory, 1993., 13
- Lanzetta, K., Yahil, A., & Fernández-Soto, A. 1996, *Nature*, 381, 759
- Legrand, F., Kunth, D., Mas-Hesse, J. M., & Lequeux, J. 1997, *A&A*, 326, 929
- Leitherer, C., Vacca, W. D., Conti, P. S., Filippenko, A. V., Robert, C., & Sargent, W. L. W. 1996, *apj*, 465, 717+
- Lowenthal, J. D. et al. 1997, *ApJ*, 481, 673
- Lu, L., Sargent, W. L. W., Barlow, T. A., Churchill, C. W., & Vogt, S. S. 1996a, *ApJS*, 107, 475+
- Lu, L., Sargent, W. L. W., Womble, D. S., & Barlow, T. A. 1996b, *ApJ*, 457, L1
- Madau, P. 1995, *ApJ*, 441, 18
- Madau, P., Ferrara, A., & Rees, M. J. 2001, *ApJ*, in Press.
- Manning, C., Stern, D., Spinrad, H., & Bunker, A. J. 2000, *ApJ*, 537, 65
- Navarro, J. F., Frenk, C. S., & White, S. D. M. 1995, *MNRAS*, 275, 720
- Oke, J. B. et al. 1995, *PASP*, 107, 375
- Pettini, M. & et al. 2001, *ApJ*, 554, 1
- Rhoads, J. E., Malhotra, S., Dey, A., Stern, D., Spinrad, H., & Jannuzi, B. T. 2000, *ApJ*, 545, L85
- Scannapieco, E. & Broadhurst, T. 2001a, *ApJ*, 550, L39
- . 2001b, *ApJ*, 549, 28
- Schneider, D. P., Schmidt, M., & Gunn, J. E. 1989, *AJ*, 98, 1951
- Spinrad, H., Stern, D., Bunker, A. J., Dey, A., Lanzetta, K., Yahil, A., Pascarelle, S., & Fernández-Soto, A. 1998, *AJ*, 116, 2617
- Squires, G., Kaiser, N., Fahlman, G., Babul, A., & Woods, D. 1996, *ApJ*, 469, 73+

- Steidel, C. C., Adelberger, K. L., Giavalisco, M., Dickinson, M., & Pettini, M. 1999, *ApJ*, 519, 1
- Steidel, C. S., Giavalisco, M., Dickinson, M., & Adelberger, K. L. 1996a, *AJ*, 112, 352
- Steidel, C. S., Giavalisco, M., Pettini, M., Dickinson, M., & Adelberger, K. L. 1996b, *ApJ*, 462, 17
- Steidel, C. S. & Hamilton, D. 1992, *AJ*, 104, 941
- Stern, D., Bunker, A., Spinrad, H., & Dey, A. 2000a, *ApJ*, 537, 73
- Stern, D., Spinrad, H., Eisenhardt, P., Bunker, A. J., Dawson, S., Stanford, S. A., & Elston, R. 2000b, *ApJ*, 533, L75
- Storrie-Lombardi, L. J., MCMahon, R. G., & Irwin, M. J. 1996, *MNRAS*, 283, L79
- Thompson, D. & Djorgovski, S. G. 1995, *AJ*, 110, 982+
- Trager, S. C., Faber, S. M., Dressler, A., & Oemler, A., J. 1997, *ApJ*, 485, 92+
- Valls-Gabaud, D. 1993, *ApJ*, 419, 7+
- Warren, S. J., Hewett, P. C., Lewis, G. F., Moller, P., Iovino, A., & Shaver, P. A. 1996, *MNRAS*, 278, 139
- Weymann, R., Stern, D., Bunker, A. J., Spinrad, H., Chaffee, F., Thompson, R., & Storrie-Lombardi, L. 1998, *ApJ*, 505, L95

Fig. 1.— Color vs. Redshift for the El, Scd and Im galaxy types of Coleman et al. (1980), the SB2 and SB3 starbursts from Kinney et al. (1996), and a B3 stellar model (Kurucz 1993). The six galaxies in our sample with measured  $(V - I)_{AB}$  color are plotted as square shaped points with error bars, or as lower limits for the galaxies at  $z=4.65$ ,  $4.87$ , and  $5.12$ . Our high- $z$  sample follows the expected color trend well. Note the potential source for confusion with elliptical galaxies at  $z \approx 1$ .

Fig. 2.— Bayesian redshift probability distributions as defined in Benítez (2000), based information from 9 optical and infrared bands in A1689. The photometric redshifts agree with the spectroscopically determined ones to the  $1\sigma$  level. There is a double peaked probability for the galaxy at  $z=5.12$ , arising from its faintness and therefore relatively large photometric errors. Note, however, that the sum of the redshift probabilities lies closest to the spectroscopic redshift.

Fig. 3.— Deep  $I$ -band image of the center of A1689 ( $z=0.18$ ) taken with LRIS, with the three high- $z$  galaxies discovered behind this cluster circled. The lensing effect is very clear, forming a general circular pattern of faint galaxies around the center of the cluster. Note the proximity of these objects to the cluster critical curve and their small lensed sizes. For reference, north is up and east is to the left.

Fig. 4.— Blue and red spectra and images of the  $z=3.77$  arc behind A1689 ( $z=0.18$ ), with the commonly found spectral features labelled. Very weak Ly- $\alpha$  emission is detected with an upper limit on its equivalent-width of  $\sim 3\text{\AA}$ . Both the Lyman-series and Lyman- $\beta$  breaks are detected, as are the interstellar lines of SiII $\lambda$ 1260, OI and SiII at  $\lambda$ 1302 and  $\lambda$ 1304 respectively, CII $\lambda$ 1336, and SiIV $\lambda$ 1398 and  $\lambda$ 1402. The sky spectrum is shown in the lower attached panels. Note this object’s arc-like shape in  $I$  and marginal detection in  $V$ .

Fig. 5.— Fluxed spectrum and images of the  $z=4.868$  galaxy behind A1689 ( $z=0.18$ ), with common spectral features marked. Strong Lyman-series and Ly- $\beta$  breaks are seen. Prominent Ly- $\alpha$  emission is detected which is asymmetric and redshifted by  $360 \text{ km s}^{-1}$  with respect to the clearly detected SiII 1260 $\lambda$  interstellar line. The dashed curve shows the bestfit unreddened B0 stellar population, and the thick solid curve, the effect of attenuation by Lyman-series blanketing. The sky spectrum is shown in the lower attached panel. Deep ground-based images in  $UBVI$  and  $J$  used for color selection show it to be small and only marginally resolved despite its proximity to the critical curve and large inferred magnification.

Fig. 6.— Spectrum and images of the  $z= 5.12$  galaxy behind A1689 ( $z= 0.18$ ), with commonly found spectral features marked. A Lyman-series break is clearly detected together with a prominent asymmetric emission line which we take to be Ly- $\alpha$  (see smoothed inset).

There is a marginally significant detection of absorption at the expected position of SiII 1260 $\lambda$ , but at this signal to noise is consistent with the continuum noise level. The sky spectrum is shown in the lower attached panel. Deep ground based images in *UBVI* and *J* used for color selection show this *V*-band dropout to be small and unresolved from the ground, despite its large inferred magnification.

Fig. 7.— One and two dimensional spectra and color image of the quadruply lensed galaxy at  $z=4.039$  behind A2390 ( $z=0.23$ ). The Lyman-series and Ly- $\beta$  breaks are clearly seen, as well as a prominent and asymmetric Ly- $\alpha$  emission line which is redshifted by 420 km s $^{-1}$  with respect to the clearly detected interstellar absorption lines of SiII 1260 $\lambda$ , OI and SiII at  $\lambda 1302$  and  $\lambda 1304$  respectively, and CII $\lambda 1336$ . The righthand panel shows the HST WFPC 2 color image, with the N and S components extending spatially 5'' and 3'' respectively. Note that the central elliptical galaxy has been removed to reveal the four individual components of this ‘extended’ Einstein cross. The elliptical is retained in the 2d spectrum in the lower panel, shown as the bright swath in between the spatially resolved N and S image components (labelled). Note the faint continuum extending toward longer wavelengths (to the right), and downward spatially from the bright Ly- $\alpha$  lines in both the N and S components, demonstrating like image parity.

Fig. 8.— Deep *I* image of the center of A2219 ( $z=0.23$ ) taken with LRIS, with the three high-*z* galaxies discovered at  $z=4.068$ ,  $z=4.445$ , and  $z=4.654$  circled and labelled. The massive cluster members lie just below center and to the right. This image forms part of a multicolor set used for photometric target selection. For reference, north is up and east is to the left.

Fig. 9.— Fluxed spectrum and images of the  $z=4.068$  galaxy behind A2219 ( $z=0.23$ ). A strong Lyman-series break is detected against a bright stellar continuum. Prominent Ly- $\alpha$  emission is seen which is asymmetric and redshifted by 830 km s $^{-1}$  with respect to the position of the several wide and nearly saturated interstellar absorption lines of SiII 1260 $\lambda$ , OI and SiII at  $\lambda 1302$  and  $\lambda 1304$  respectively, CII $\lambda 1336$ , and SiIV $\lambda 1398$  and  $\lambda 1402$ . The dashed curve shows the bestfit unreddened B5 stellar population, and the thick solid curve, the effect of attenuation by Lyman-series blanketing and absorption at the position of Ly- $\alpha$  ( $\log N = 21.1$ ). The sky spectrum is included in the bottom attached panel. Two deep *VI* Keck images show that this *V*-band dropout is only marginally resolved from the ground.

Fig. 10.— Fluxed spectrum and images of the  $z= 4.445$  galaxy behind A2219 ( $z=0.23$ ). A strong Lyman-series break is detected against a bright stellar continuum. Prominent Ly- $\alpha$  emission is seen which is asymmetric and redshifted by 700 km s $^{-1}$  with respect to the position of the several clearly detected interstellar absorption lines of SiII 1260 $\lambda$ , OI and SiII at  $\lambda 1302$  and  $\lambda 1304$  respectively, CII $\lambda 1336$ , and SiIV $\lambda 1398$  and  $\lambda 1402$ . The dashed curve shows the

bestfit unreddened B3 stellar population, and the thick solid curve, the effect of attenuation by Lyman-series blanketing and absorption at the position of Ly- $\alpha$  ( $\log N = 21.1$ ). The 2d spectrum is shown in the lower panel. Note the spatially resolved Ly- $\alpha$  line, and continuum extending toward longer wavelengths (to the right). The sky spectrum is included in the bottom attached panel. Two deep *VI* Keck images show this *V*-band dropout to be resolved but small.

Fig. 11.— Fluxed spectrum and images of the  $z= 4.654$  galaxy behind A2219 ( $z=0.23$ ). Strong Lyman-series and Ly- $\beta$  breaks are seen together with prominent Ly- $\alpha$  emission redshifted by  $425 \text{ km s}^{-1}$  with respect to the clearly detected SiII  $1260\lambda$  interstellar line. The dashed curve shows the bestfit unreddened B3 stellar population, and the thick solid curve, the effect of attenuation by Lyman-series blanketing and absorption at the position of Ly- $\alpha$  ( $\log N = 21.5$ ). The sky spectrum is included in the bottom attached panel. Two deep *VI* Keck images show that this *V*-band dropout is only marginally resolved from the ground.

Fig. 12.— Spectrum and images of the  $z= 4.248$  galaxy behind AC114 ( $z=0.31$ ). A strong Lyman-series break is detected against a bright stellar continuum. Ly- $\alpha$  is seen in emission redshifted by  $460 \text{ km s}^{-1}$  with respect to the position of the interstellar absorption line SiII  $1260\lambda$ , at the  $2\sigma$  level. The sky spectrum is included in the bottom attached panel. Two deep *BI* images show this *B*-band dropout to be small and only marginally resolved.

Fig. 13.— The Ly- $\alpha$  emission line is plotted for each of the high- $z$  galaxies discovered (solid), along with the expected location of the center of Ly- $\alpha$  emission based on the redshift measured from the absorption lines (dashed). A systematic bias is apparent which is interpreted as evidence for gas outflow. Note that for the galaxy at  $z=5.120$ , the continuum emission is too weak for reliable absorption line detection.

Fig. 14.— The blueshift of the metal lines relative to the centroid of the Ly- $\alpha$  emission is plotted against the summed rest equivalent width of two lines: OI  $1302\lambda$  and SiIV  $1304\lambda$ . The data for the five emission line objects discovered in our survey with measurable absorption line equivalent widths are shown as circles and their redshifts marked. The other symbols correspond to different sets of data for high- $z$  and local galaxies (see legend). The increasing trend may be attributed to a dispersion in gas outflow speed for saturated interstellar lines, as discussed in the text.

Fig. 15.— The blueshift of the metal lines relative to the centroid of the Ly- $\alpha$  emission is plotted against the summed rest equivalent width of several lines: SiII  $1260\lambda$ , OI and SiII at  $\lambda 1302$  and  $\lambda 1304$  respectively, and CII  $\lambda 1336$ . The data for the five emission line objects with measurable absorption line equivalent widths for all of these lines are shown as circles and their redshifts labelled. The other symbols correspond to different high- $z$  and local

starburst galaxies (see legend). As in Fig. 14, the clear increasing trend may be attributed to a dispersion in gas outflow speed for saturated interstellar lines.

Fig. 16.— Rest equivalent width of Ly- $\alpha$  emission as a function of redshift. Although the scatter is large, a rough increasing trend is seen, which may be a genuine evolutionary effect towards younger stellar populations at high redshift with less luminous stellar continua, although larger samples are required for a more well constrained measurement.

Table 1. Distant Galaxy Imaging Information

Cluster	Position (J2000)	$I_{AB} \pm 1\sigma$	$(V - I)_{AB}$	Size (kpc h <sup>-1</sup> )
A1689_1	(13:11:29.980,-1:19:15.293)	$24.2 \pm 0.2$	1.5	2
A2390_1	(21:53:33.669,17:42:04.184)	$23.0 \pm 0.3$		1
A2219_1	(16:40:12.638,46:44:59.412)	$24.1 \pm 0.2$	1.8	3.5
AC114_1	(22:58:45.841,-34:49:33.806)	$23.9 \pm 0.3$		<2
A2219_2	(16:40:15.885,46:43:58.696)	$23.7 \pm 0.2$	1.8	3
A2219_3	(16:40:11.152,46:41:58.343)	$24.9 \pm 0.2$	> 2.1 <sup>b</sup>	<2
A1689_2	(13:11:25.499,-1:20:51.900)	$23.3 \pm 0.1$	> 3.2 <sup>a</sup>	1.5
A1689_3	(13:11:35.042,-1:19:51.617)	$25.0 \pm 0.2$	> 1.5 <sup>a</sup>	<0.5

Note. — The columns are: Cluster; Object Coordinate (J2000);  $I_{AB}$  magnitude with  $1\sigma$  error bars;  $(V - I)_{AB}$  color; Intrinsic Object Size, in kpc h<sup>-1</sup> for  $\Omega = 0.3$ , and  $\Lambda = 0.7$ .

<sup>a</sup> $2\sigma$  limiting magnitude is  $V_{AB} = 26.5$

<sup>b</sup> $2\sigma$  limiting magnitude is  $V_{AB} = 27.0$

Table 2. Distant Galaxy Spectral Information

Cluster	$z$ $\pm 0.001$	$W_\alpha$ ( $\text{\AA}$ )	$W_1$ ( $\text{\AA}$ )	$W_2$ ( $\text{\AA}$ )	$\Delta V$ ( $\text{km s}^{-1}$ )
A1689_1	3.770	$\leq 3.3$	3.4	7.1	
A2390_1	4.039	$8.84^{+5.5}_{-2.5}$	1.3	6.1	$420 \pm 100$
A2219_1	4.068	$5.05^{+2.1}_{-2.2}$	5.9	13.8	$830 \pm 100$
AC114_1	4.248	$3^{+2.4}_{-1.6}$			
A2219_2	4.445	$9.05^{+4.6}_{-3.3}$	3.8	10.4	$700 \pm 90$
A2219_3	4.654	$10.4^{+6.8}_{-5.5}$	1.8	5.7	$425 \pm 120$
A1689_2	4.868	$12.4^{+8.83}_{-3.84}$	2.1	5.7	$360 \pm 120$
A1689_3	5.120	$29.7^{+13.29}_{-4.6}$			

Note. — The columns are: Cluster; Redshift (not heliocentric corrected); Rest Equivalent Width of Ly- $\alpha$ ; Summed rest equivalent width of OI 1302 $\lambda$  + SiII 1304 $\lambda$ ; Summed rest equivalent width of SiII 1260 $\lambda$  + OI 1302 $\lambda$ + SiII 1304 $\lambda$  + CII 1336 $\lambda$ ; Velocity Shift between the centroid position of Ly- $\alpha$  and the position of the interstellar lines, with  $1\sigma$  error bars



### Color-redshift Relationship

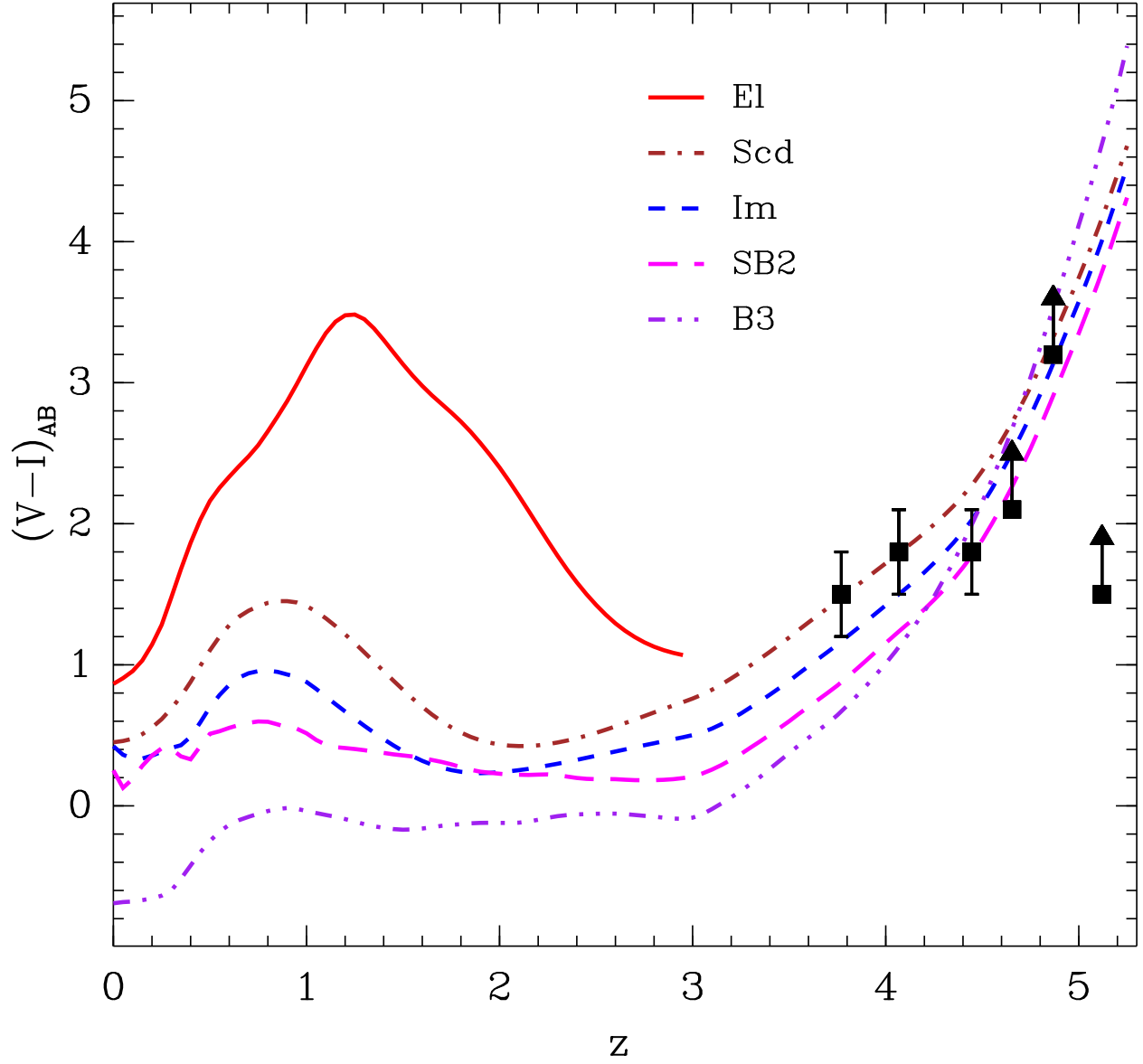


### Photo-z Probability Distribution

